A Multi-Tooth Interactive Flux Reversal Permanent Magnet Motor

Mohammad Amin Jalali Kondelaji, Mohammad Reza Sarshar, Pedram Asef, *Senior Member, IEEE*
Mojtaba Mirsalim, *Life Senior Member, IEEE*

***Abstract*—This article proposes a novel multi-tooth interactive flux reversal permanent magnet (IFRPM) motor. The innovative motor design incorporates both tooth and yoke PMs, providing both flux reversal (FR) and biased flux (BF) effects, respectively. The former directly contributes to torque production and an increase in air-gap flux density, while resulting in a decrease in stator-pole flux. Using flux modulation theory (FMT), the influence of each harmonic on the torque generation is analyzed. The motor's dimensions are optimized using a genetic algorithm to achieve the maximum torque while minimizing the torque ripple. Four benchmark motors two with FR effect and two with BF effect-are used for comparison. The findings underscore the superior performance of the IFRPM. First, the IFRPM reduces saturation levels compared to BF motors. Additionally, a torque quality factor (TQF) is introduced, which considers the average torque, torque ripple, and PM volume, providing a fair evaluation. The IFRPM achieves a 669% and 95% improvement in TQF over recent FRPMs of similar size, respectively. It offers at least a 318% higher TQF than BF motors. Furthermore, the IFRPM exhibits the lowest torque ripple in overload conditions. Finally, the motor is prototyped and experimentally validated.**

***Index Terms*—Biased flux motor, flux reversal motor, finite element analysis, multi-tooth structure, torque quality.**

I. Introduction

BY combining switched reluctance motors (SRMs) and flux modulation permanent magnet (PM) machines, stator-PM motors have emerged in various applications, such as electrified transportation, due to their intrinsic high torque density [1], [2]. Additionally, stator-PM topologies offer greater diversification of PM arrays compared to rotor-PM types, thanks to superior thermal management and the elimination of vibration and centrifugal forces in the rotor. This protective environment for PMs can significantly enhance the durability of rare-earth PMs, providing a robust solution for long-lasting performance [3].

The diverse arrangements of PMs in the stator yield three significant effects: flux switching (FS) [4], biased flux (BF) [5], and flux reversal (FR) [6]. In electric motors with the FS effect (FSPMs), the armature winding sandwiches the tangentially magnetized PMs to benefit from the spoke-PM flux concentration effect [4]. However, placing the PMs in the center of the heat source accelerates the demagnetization risk. In the BF effect, the PMs are located between two adjacent stator poles, either in yoke or slot, to alleviate the demagnetization risk. Different topologies are introduced according to the stator core shape, benefiting from the BF effect. An inter-modular PM motor (IMPM) is proposed in [7], where spoke PMs are parked between the E-core stator modules. Furthermore, a biased-flux PM motor (BFPM) with slot and yoke PMs is introduced in [8] to improve the saturation risk by interacting two PM arrays.

In flux reversal PM machines (FRPMs), radially magnetized PMs are placed on or between the stator teeth or within the slot opening and bring four-quadrant energy conversion to conventional stator-PM motors. This arrangement significantly boosts the air gap flux density, leading to increased torque [9]. In conventional FRPMs, PMs with the opposite magnetization direction are parked adjacent to each other [10], which often results in high flux leakage. To tackle this issue, consequent-pole (CP) design replaces half of the PMs with iron teeth to effectively reduce leakage [11]. The CP pattern not only decreases the PM volume by 50%, but also significantly improves the output torque [9], [12]. This improvement is mainly driven by shortening the effective air gap and paralleling the PM's and armature's flux [13]. The Halbach PM array in slot opening is proposed in [14], [15] to achieve the flux focusing effect while minimizing the leakage.

An asymmetric PM array is developed in [16] to reduce the interpolar flux leakage and improve torque. A hybrid-excited FRPM motor with an asymmetric CP design is investigated in [17], [18] to increase the flux linkage and mitigate the saturation of the stator pole. Moreover, split-tooth FRPMs offer a solution for flux leakage reduction and magnetic field modulation, resulting in higher torque production and flux regulation [19]. In reference [20], the asymmetric CP-FRPM topology is introduced to reveal that a split-tooth structure can potentially increase the torque and decrease the torque ripple. Additionally, to benefit from the features of both the FR and FS effects, a synergistic stator-PM motor is proposed in [21]. Demonstrating a remarkable 20% increase in torque compared to FSPM. An innovative E-core FSPM with FR effect is investigated in [22], showcasing its impressive bidirectional flux enhancement across multiple working harmonics.

This work introduces a novel multi-tooth interactive flux

Mohammad Amin Jalali Kondelaji and Pedram Asef are with the Advanced Propulsion Laboratory (APL) and the e-Motion Laboratory, Mechanical Engineering Department, University College London (UCL), London, WC1E 7JE, UK. (e-mail: amin.jalali@ucl.ac.uk, pedram.asef@ucl.ac.uk).

Mohammad Reza Sarshar and Mojtaba Mirsalim are with the Electrical Machines and Transformers Research Laboratory (EMTRL), Department of Electrical Engineering, Amirkabir University of Technology (Tehran Polytechnic), Tehran 15916, Iran. (e-mail: rezasarshar@aut.ac.ir, mirsalim@aut.ac.ir).

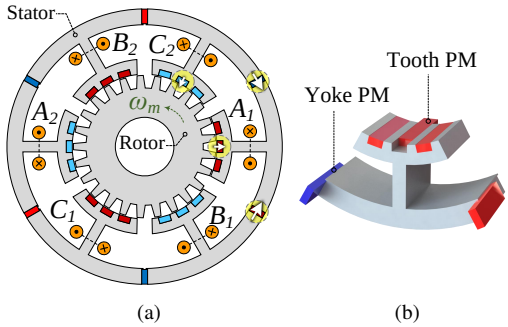

Fig. 1. Structure of the proposed IFRPM motor. (a) Cross-section view. (b) A stator module with tooth and yoke PMs.

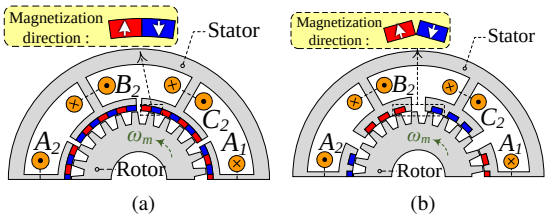

Fig. 2. Structures of the benchmark motors with flux reversal (FR) effect. (a) Conventional FRPM. (b) Consequent-pole FRPM (CPFRPM).

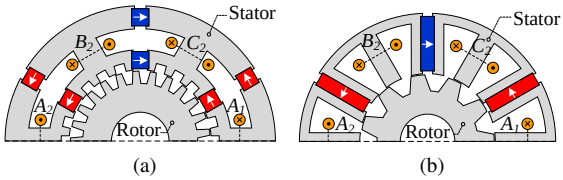

Fig. 3. Structures of the benchmark motors with biased-flux (BF) effect. (a) BFSPM [8]. (b) IMPM [7].

TABLE I
MAIN PARAMETERS AND DIMENSIONS OF THE FIVE MOTORS.

Basic Design Parameter		IFRPM	FRPM	CPFRPM	BFSPM	IMPM
Stator outer radius (mm)	R_o	47				
Rotor shaft radius (mm)	R_{sh}	10				
Electric frequency (Hz)	f	166.67				
Rated speed (rpm)	ω_m	400				900
Stack length (mm)	l_{st}	20				
Air gap length (mm)	l_g	0.4				
Current density (A/mm^2)	δ	6				
Number of stator pole	N_{sp}	6				
Number of rotor teeth	N_{rt}	25				11
PM type (B_r , μ_r @ 20°C)		NdFeB-N42 (1.31T, 1.08)				
Core material		M470-50A, Knee point: 1.6T				
PM volume (cm^3)	V_{PM}	4.16	6.02	2.96	6.00	8.64

reversal PM (IFRPM) motor. The motor utilizes two distinct arrays of PMs: CP PMs with the FR effect and yoke PMs which incorporate the BF effect. The synergy between these PMs results in remarkably higher torque production and reduced torque ripple, as explored in the following sections. In Section II, the proposed IFRPM is described, together with four benchmark motors with only FR and BF effects and research contributions are highlighted. To investigate the contributions of the interactive PMs, flux modulation theory (FMT) is developed in Section III to disclose the working harmonics. In Section IV, the motor dimensions, along with those of the benchmark motors, are optimized using a GA, followed by simulation results and a comparison with the four benchmark motors. Experimental verification is provided in Section V to validate the simulation outcomes. Finally, a conclusive summary of the findings is outlined in Section VI.

II. MOTOR TOPOLOGY AND BENCHMARK MOTORS

A. Proposed Motor Configuration

Fig. 1a depicts the structure of the IFRPM with the asymmetric CP array, where the stator teeth sandwich the tooth PMs. Fig. 1b illustrates the placement of homopolar PMs on each stator module, with PMs of opposite magnetization directions positioned on adjacent modules. This configuration effectively introduces the FR effect to the motor. The yoke PMs are arranged alternately homopolar to benefit from the flux-concentrating effect and add the BF effect to the structure. Two stator-PM motors with only the FR effect and two with the BF effect are selected from the literature to unveil the improvements of the IFRPM's structure. A conventional FRPM motor is presented in Fig. 2a. Fig. 2b highlights the innovative multi-tooth topology featuring an asymmetric CP design. Additionally, two benchmark motors with the BF effect are illustrated in Fig. 3, providing a compelling basis for comparison. The first benchmark motor featuring the BF effect is the multi-tooth biased-flux slot PM (BFSPM) motor, as illustrated in Fig. 3a [8]. The second is the modular E-core motor equipped with inter-modular PMs (IMPM), depicted in Fig. 3b [7]. The main parameters and dimensions of all structures are listed in Table I. For a fair comparison, all motors have the same outer diameter, stack length, current density, and operating frequency. Given the current density $(6A/mm^2)$, which falls within the medium range [7], natural cooling is applied for all motors. The five motors under comparison have nearly the same specific electric loading.

Integrating the BF effect into the FRPM motor creates a dynamic interplay between the two PM arrays. This synergy brings about two major enhancements in motor performance compared to traditional FRPM and BFPM designs: (1) it lowers the flux density at the stator poles, mitigating the risk of saturation, and (2) the addition of yoke PMs enhances the air gap flux density, resulting in a higher torque.

B. Research Contributions

The primary contribution of the IFRPM motor is the incorporation of yoke PMs into the multi-tooth CPFRPM structure and is shown in Fig. 4. This configuration enhances the magnetic interaction within the stator, leading to improved performance characteristics. The tooth PMs introduce the FR effect into the multi-tooth structure, enabling four-quadrant energy conversion. The FR effect directly enhances the air-gap flux density and improves torque production. However, the key novelty of IFRPM lies in the integration of the BF effect into the FRPM configuration, which reduces the risk of saturation and further increases the air-gap flux density.

The predicted flux lines for the benchmark CPFRPM motor are illustrated in Fig. 4a. In the proposed design, yoke PMs

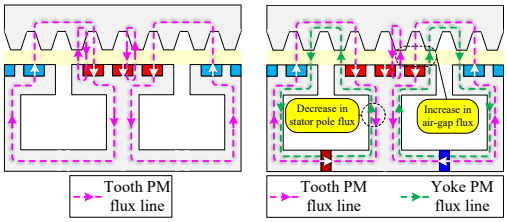

Fig. 4. Predicted no-load flux lines for (a) CPFRPM and (b) IFRPM.

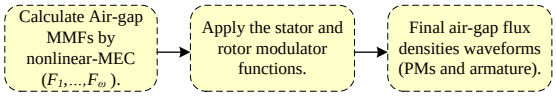

Fig. 5. Procedure of analytical method based on nonlinear-MEC.

are incorporated to produce a stator flux that counteracts the stator pole flux generated by the tooth PMs. This magnetic interaction leads to a reduction in the flux density at the stator poles. In contrast, beneath the stator teeth that are not equipped with PMs, this interaction results in an increase in the air-gap flux density (see Fig. 4b). The main improvements of the proposed IFRPM can be summarized as follows:

- Compared to CPFRPM, IFRPM reduces the stator pole flux density by 67%, lowering the risk of saturation.
- The air-gap flux density and its working harmonics are enhanced compared to the conventional structure.
- Compared to the BFPM motors, the PM volume is reduced while maintaining comparable average torque.

III. Harmonic Analysis

The flux modulation theory (FMT) is conducted under two no-load and amature-excited conditions to investigate the harmonic components of the motor and their contribution in back-EMF and torque generation. The general procedure of the analytical method is illustrated in Fig. 5.

A. No-load FMT

No-load FMT is applied to determine each PM array's harmonics. The primitive magneto-motive force (MMF) functions for each PM array in the air gap, where the rotor is considered flat, are illustrated in Fig. 6a. Under the stator teeth, the flux density is improved by adding F_{yPM} to F_{tPM}. Also, the interaction between these two arrays reduces the stator pole's flux density and lowers the saturation risk. Fourier series expansion for the yoke and tooth PM's primitive MMF functions are derived in (1) and (2), respectively.

$$\begin{cases} F_{yPM}(\theta) = \sum_{n=odd}^{\infty} b_n \sin(nN_{PM}\theta) \\ b_n = \frac{16}{n\pi}\sin(\frac{n\pi}{2}) \times \left(\cos\left(\frac{nN_{PM}}{2}(\theta_{smt}+\theta_{tPM})\right)\right. \\ \quad \times \cos\left(nN_{PM}(\theta_{smt}+\theta_{tPM})\right) \times F_1 \sin(\frac{nN_{PM}\theta_{smt}}{2}) \\ \quad \left. + \frac{F'_1}{4}\cos\left(n\,N_{PM}\,\theta_{tPM}\right)\right) \end{cases} \quad (1)$$

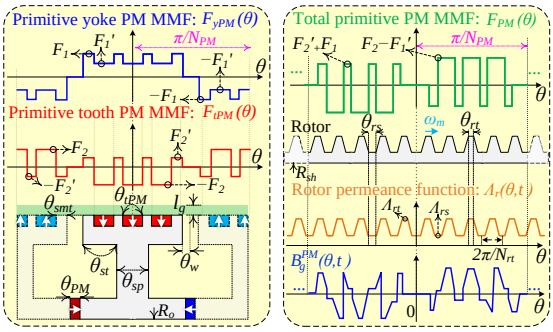

Fig. 6. No-load FMT. (a) The primitive MMF functions with a flat rotor. (b) Final air gap flux density modulated with rotor permeance function.

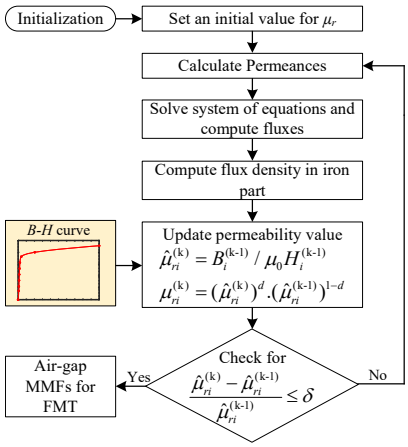

Fig. 7. The flowchart of air-gap MMFs calculation.

$$\begin{cases} F_{tPM}(\theta) = \sum_{n=odd}^{\infty} c_n \sin(nN_{PM}\theta) \\ c_n = \frac{16}{n\pi}\sin(\frac{n\pi}{2}) \times \left(\cos\left(\frac{nN_{PM}}{2}(\theta_{smt}+\theta_{tPM})\right)\right. \\ \quad \times \cos\left(nN_{PM}(\theta_{smt}+\theta_{tPM})\right) \times F_2 \sin(\frac{nN_{PM}\theta_{smt}}{2}) \\ \quad \left. - \frac{F'_2}{4}\cos\left(n\,N_{PM}\,\theta_w\right)\right) \end{cases} \quad (2)$$

where F_1, F_2, F'_1, and F'_2 denote the amplitudes of the MMFs as presented in Fig. 6. The motor sizing parameters are illustrated in Fig. 6. To obtain a precise calculation of the air-gap MMFs, an initial value of permeability is first assigned for the reluctance calculation in the applied magnetic equivalent circuit (MEC), and parameters such as MMFs and flux density are computed. Using the resulting flux density and the B-H curve, the permeability value is updated and reassigned to the reluctance calculation, and the MMF values are updated accordingly. This iterative process continues until the difference in permeability between iterations is less than δ. The influence of the B-H curve and magnetic saturation is illustrated in Fig. 7. By operating a superposition on the primitive MMFs, the total primitive PM MMF is expressed as:

$$F_{PM}(\theta) = F_{yPM}(\theta) + F_{tPM}(\theta). \quad (3)$$

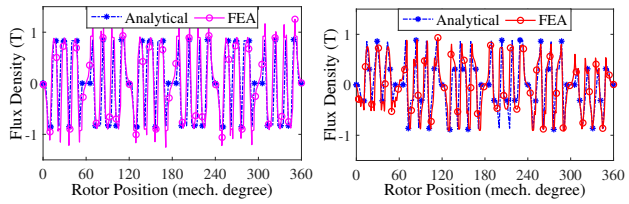

Fig. 8. FEA and analytical no-load air gap flux densities caused by the PMs. (a) Without rotor modulator. (b) With rotor modulator.

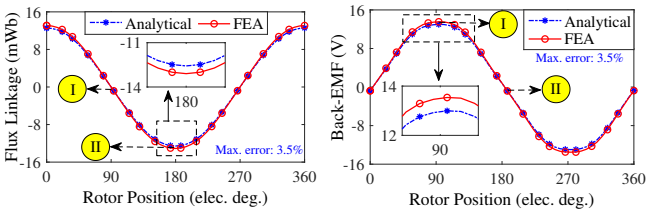

Fig. 9. FEA and analytical (a) flux linkage and (b) back-EMF profiles.

It is worth noting that the primitive function repeats every π/N_{PM}, and according to the asymmetric PM arrangement, N_{PM} is equal to 3. Next, F_{PM} is exposed to the rotor permeance function, which considers the effect of the rotor saliency and can be expressed as:

$$\Lambda_r(\theta,t)=\sum_{j=0}^{\infty}\Lambda_{rj}\cos(\,jN_{rt}(\theta-\omega_m t-\theta_{r0})), \tag{4}$$

where for each j, Λ_{rj} is obtained as:

$$\begin{cases} j=0\rightarrow\Lambda_{rj}=\Lambda_{r0}=\dfrac{N_{rt}}{\pi}(\Lambda_{rt}\theta_{rt}+\Lambda_{rs}\theta_{rs}) \\ j\neq 0\rightarrow\Lambda_{rj}=\dfrac{2}{j\pi}(\Lambda_{rt}-\Lambda_{rs})\times\sin(jN_{rt}\dfrac{\theta_{rt}}{2}). \end{cases} \tag{5}$$

The final no-load curve (B_g^{PM}) is obtained by the product of (3) and (4) and drawn in Fig. 6b. B_g^{PM} is derived as:

$$\begin{cases} B_g^{PM}(\theta,t)=F_{PM}(\theta)\times\Lambda_r(\theta,t)= \\ \displaystyle\sum_{n=odd}^{\infty}\sum_{j=0}^{\infty}a_n\sin\left((nN_{PM}+jN_{rt})\theta-jN_{rt}(\omega_m t+\theta_{r0})\right) \\ +\displaystyle\sum_{n=odd}^{\infty}\sum_{j=0}^{\infty}a_n\sin\left((nN_{PM}-jN_{rt})\theta+jN_{rt}(\omega_m t+\theta_{r0})\right) \end{cases} \tag{6}$$

where $a_n=\frac{(b_n+c_n)\times\Lambda_{rj}}{2}$. The comparison of FEA and analytical waveforms for the total primitive PM MMF and flux density curve is drawn in Figs. 8a and 8b, respectively, which verify a good precision of the analytical FMT.

The no-load FMT will continue to calculate the flux linkage and back-EMF. The winding function Fourier series expansion can be written as:

$$\begin{cases} N_\omega(\theta)=\displaystyle\sum_{i=0}^{\infty}N_i\cos(iP_a\theta) \\ N_i=\dfrac{N_c P_a\theta_{sp}}{\pi},\ i=0, \\ N_i=\dfrac{2N_c}{i\pi}\sin(iP_a\dfrac{\theta_{sp}}{2}),\ i\neq 0 \end{cases} \tag{7}$$

The flux linkage is obtained from the integral of the product of B_g^{PM}, the effective air gap area (A), and the winding function (N_w). Also, the back-EMF is derived in (8) and (9). The accuracy of the analytical flux linkage and back-EMF curves are illustrated in Figs. 9a and 9b, respectively, where the analytical model shows a maximum error of 3.5%.

$$e(t)=-\frac{d}{dt}\psi(t)=-\frac{d}{dt}(\int_0^{2\pi}N_\omega(\theta).A.B_g^{PM}(\theta,t)d\theta) \tag{8}$$

B. Armature FMT

The armature FMT process is divided into three levels, as shown in Fig. 10a. First, the stator and rotor are considered flat, and the primitive MMF functions for the three phases are demonstrated by F_A, F_B, and F_c. Also, the primitive resultant armature MMF F_s and it's coeffiecient F_{sk} are obtained by the superposition of the primitive MMF functions and can be expressed as:

$$\begin{aligned} F_s(\theta,t)=&\sum_{k=3d-2}^{\infty}F_{sk}\cos(kP_a\theta-N_{rt}\omega_m t) \\ &+\sum_{k=3d-1}^{\infty}F_{sk}\cos(kP_a\theta+N_{rt}\omega_m t), \end{aligned} \tag{10}$$

$$\begin{aligned} F_{sk}=\frac{3}{4\pi k}\times&\left(2\sin\left(kP_a(\frac{\pi}{N_{PM}P_a}-\theta_w)\right)\right. \\ &\left.-\sin\left(kP_a(\frac{\pi}{P_a}+\theta_w)\right)+\sin\left(kP_a(\frac{\pi}{N_{PM}P_a}-\theta_w)\right)\right) \end{aligned} \tag{11}$$

Next, F_s is modulated by only the stator teeth. The stator modulator function is given in (12). The product of F_s and M_s is the stator-modulated MMF function F_{sm}. Also, M_{sm} represents the Fourier series coefficient of the stator modulator function. However, it cancels out in the final calculation as the period of F_s is a multiple of the period of M_s.

$$M_s(\theta)=M_{s0}+\sum_{m=1}^{\infty}M_{sm}\cos(m\frac{N_{PM}}{2}\theta) \tag{12}$$

$$M_{s0}=\frac{N_{PM}}{\pi}\left(2\theta_{smt}+\frac{3h_{st}\times\theta_{tPM}}{2(h_{st}+h_t)}\right) \tag{13}$$

The stator-modulated MMF function is modulated by the rotor permeance function in (14), forming the final waveform of the air gap flux density generated by the armature B_g^{Arm}. The Fourier series expansion of B_g^{Arm} is calculated in (15).

$$B_g^{Arm}(\theta,t)=\underbrace{F_s(\theta,t)\times M_s(\theta)}_{F_{sm}(\theta,t)}\times\Lambda_r(\theta,t) \tag{14}$$

$$e(t)=\sum_{i=0}^{\infty}\sum_{n=odd}^{\infty}\sum_{j=0}^{\infty}\begin{cases}\dfrac{N_iA(b_n+c_n)\Lambda_{rj}jN_{rt}\omega_m}{2\left|nN_{PM}-jN_{rt}\right|}\sin(jN_{rt}(\omega_m t+\theta_{r0})), & \left|nN_{PM}-jN_{rt}\right|=iP_a\\ \dfrac{-N_iA(b_n+c_n)\Lambda_{rj}jN_{rt}\omega_m}{2(nN_{PM}+jN_{rt})}\sin(jN_{rt}(\omega_m t+\theta_{r0})), & nN_{PM}+jN_{rt}=iP_a\end{cases} \tag{9}$$

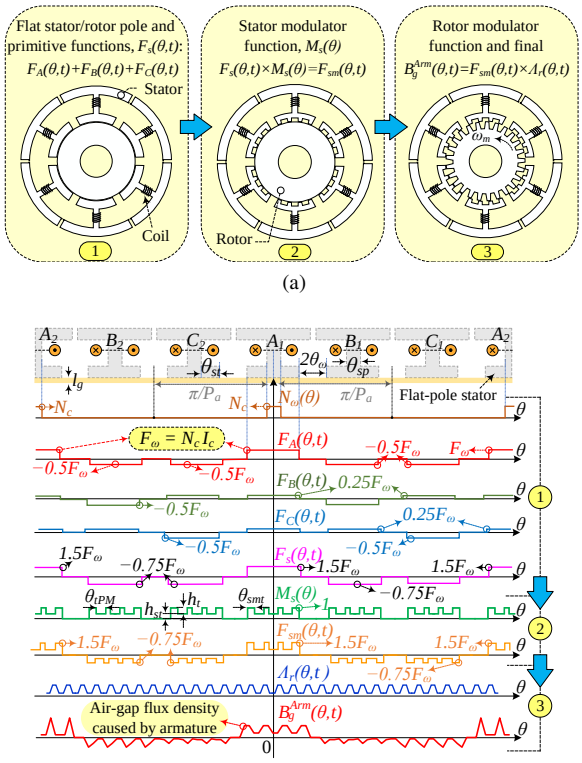

Fig. 10. FMT process of the air gap flux density caused by the armature. (a) The accurate motor shape in each level. (b) The functions.

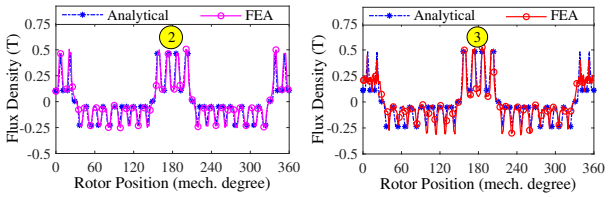

Fig. 11. FEA and analytical air gap flux densities caused by the armature. (a) Without rotor modulator. (b) With rotor modulator.

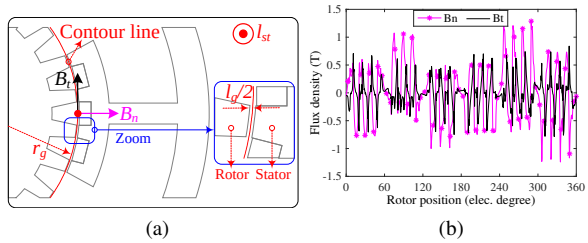

Fig. 12. (a) Maxwell's stress tensor parameters. (b) Normal and tangential components of air-gap flux density waveforms.

TABLE II
QUANTITATIVE COMPARISON OF ANALYTICAL AND FEA RESULTS.

	No-load Air-gap Flux Density (T)			Armature Air-gap Flux Density (T)		
Rotor position (Deg)	Analytical	FEA	Error (%)	Analytical	FEA	Error (%)
0°	0.00	0.01	-	0.17	0.18	3.3
30°	0.73	0.75	2.8	0	0.04	-
60°	0.01	0.01	0	-0.06	-0.07	3.5
90°	-0.73	-0.71	3.3	-0.05	-0.04	3.4
120°	0	0	0	-0.05	-0.04	3.1

To validate the accuracy of the armature Flux Modulation Theory (FMT) model, we compared the analytical and FEA-obtained flux density curves at levels 2 and 3, as depicted in Figs. 11a and 11b. The comparison reveals a strong agreement between the analytical and FEA waveforms at most points, underscoring the reliability of the FMT process. The point-to-point comparison between FMT and FEA shows that the analytical model accurately predicts both no-load and armature air-gap flux densities, with deviations below 3.5%, thereby validating the proposed approach (Table II).

C. Working Harmonics Analysis

In the final step of the FMT process, the no-load MMF harmonics are grouped based on their mechanical speed as listed in Table III. Each group has either a positive or negative contribution to back-EMF and torque generation. Based on the mechanical speeds, the rotation direction of these harmonics in the air gap can be static, forward, or backward. One notable point is that the harmonic orders can be generated by different pole-pair numbers (PPNs); however, according to analytical functions, the predominant influence in generating these harmonics comes from the pole-pair numbers with smaller Fourier series components n and j. Therefore, the harmonic orders are assigned to the groups with the PPNs that have smaller component amplitudes. The synchronous no-load and armature flux density harmonics with the same orders are involved in torque production. Table III shows the contribution of each harmonic order to back-EMF and torque generation obtained from the Maxwell's stress tensor. The backward group has the largest contribution in back-EMF generation. Although static harmonics do not contribute to back-EMF generation, they have the largest share of 80% in torque production.

Applying Maxwell's stress tensor (16) to the proposed motor can analyze and calculate the generated torque caused by air-gap flux density working harmonics.

$$T_{ei}=\frac{\pi r_g^2 l_{st}}{\mu_0}B_{ni}B_{ti}\cos(\theta_{ni}-\theta_{ti}), \tag{16}$$

In (16), T_{ei} and r_g show the torque of i^{th} harmonic and the air-gap radius, and B_{ni}, B_{ti}, θ_{ni}, and θ_{ti} are the amplitudes and phase angles of the i^{th} harmonic for the radial (normal) and tangential components, respectively.

$$B_g^{Arm}(\theta,t)=\sum_{j=0}^{\infty}\sum_{k=3d-1,k=3d-2}^{\infty}\frac{F_{sk}M_{s0}\Lambda_{rj}}{2}\cos\left((kP_a+jN_{rt})\left(\theta-\frac{(j\mp1)N_{rt}\omega t+jN_{rt}\theta_{ro}}{kP_a+jN_{rt}}\right)\right)$$
$$+\sum_{j=0}^{\infty}\sum_{k=3d-1,k=3d-2}^{\infty}\frac{F_{sk}M_{s0}\Lambda_{rj}}{2}\cos\left((kP_a-jN_{rt})\left(\theta+\frac{(j\pm1)N_{rt}\omega t+jN_{rt}\theta_{ro}}{kP_a-jN_{rt}}\right)\right) \quad (15)$$

TABLE III
HARMONIC GROUPS AND CONTRIBUTIONS OF PREDOMINANT HARMONIC ORDERS IN BACK-EMF AND TORQUE GENERATION.

Group	Pole-pair number	Mechanical speed	Direction	Harmonic number	B_g^{PM}	Back-EMF	Torque Contribution
G1	nN_{PM}	0	Static	9 (n=3)	0.10 T		0.3%
				15 (n=5)	0.21 T		3.9%
				21 (n=7)	0.43 T	-	21.6%
				27 (n=9)	0.47 T		54.5%
				51 (n=17)	0.05 T		0.08%
G2	$nN_{PM}+jN_{rt}$	$\frac{jN_{rt}\omega_m}{nN_{PM}+jN_{rt}}$	Forward	40 (n=5,j=1)	0.05 T	-0.33 V	1.14%
				46 (n=7,j=1)	0.09 T	-0.50 V	2.42%
				52 (n=9,j=1)	0.05 T	-0.25 V	0.8%
G3	$nN_{PM}-jN_{rt}>0$	$\frac{-jN_{rt}\omega_m}{nN_{PM}-jN_{rt}}$	Backward	2 (n=9,j=1)	0.05 T	6.59 V	-5.5%
G4	$nN_{PM}-jN_{rt}<0$	$\frac{jN_{rt}\omega_m}{-nN_{PM}+jN_{rt}}$	Forward	4 (n=7,j=1)	0.07 T	4.63 V	4.8%
				10 (n=5,j=1)	0.05 T	1.30 V	2.74%

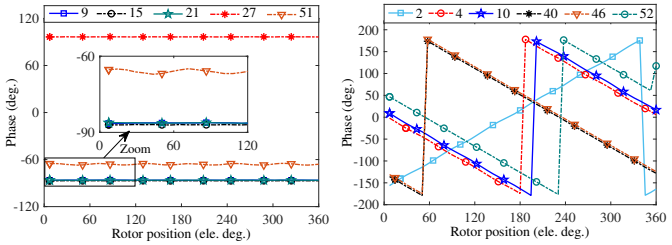

(a) (b)

Fig. 13. Phase vs. rotor position for (a) static and (b) rotating harmonics.

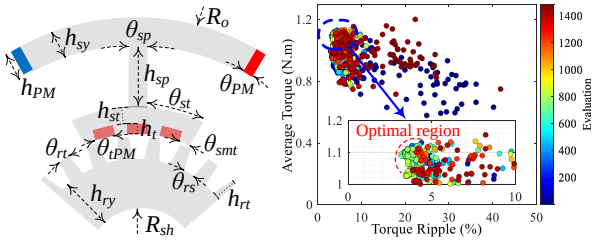

(a) (b)

Fig. 15. (a) Optimization parameters. (b) Convergence profile.

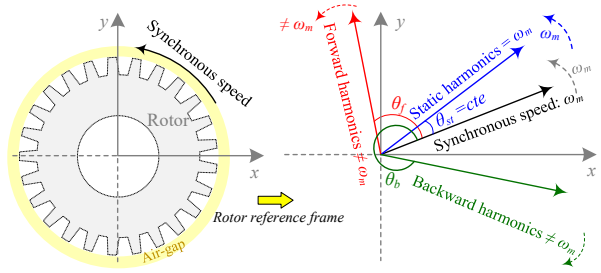

Fig. 14. Speed and direction of each harmonic group.

The parameters in Maxwell's stress tensor equation are shown in Fig. 12a. The surface where the normal and tangential components of the air-gap flux density are measured is located at the air-gap's center, equidistant from the stator and the rotor by $l_g/2$. Fig. 12b also shows the waveforms of the normal and tangential components.

Since the 2^{nd} harmonic has a negative rotational direction, it generates a corresponding torque contribution. Additionally, the static harmonics, particularly those of orders 21 and 27, contribute more than 80% of the total harmonic impact, as detailed in Table III. Also, given that the majority of torque production, approximately 75%, is contributed by only two harmonic orders (21st and 27th), the torque generation is effectively governed by these two components. It is noteworthy that the static harmonics in the proposed IFRPM, which are primarily responsible for torque production (approximately 80% of the full-load torque, see Table III, appear stationary from the rotor's reference frame, i.e., they have zero relative speed with respect to the rotor. However, from the perspective of a stationary observer, these harmonics rotate in the air gap at synchronous speed. The phase versus rotor positions of the static harmonics are shown in Fig. 13a (with negligible fluctuations), for normal components. It is clear that the phases of the static harmonics remain constant with rotor rotation, showing synchronous speed, in contrast to the rotating harmonics, whose phases fluctuate, as demonstrated in Fig. 13b. For better comprehension, the direction and speed of each harmonic group are shown in Fig. 14. The number of interacting harmonic pairs is significantly reduced, which effectively contributes to the mitigation of torque ripple.

The FMT model is used to analytically attribute and trace the harmonics of the normal air-gap flux density and back-EMF, while the Maxwell stress tensor, fed by FMT-derived B_n and FEA-based B_t, is employed independently to quantify the torque contributions by harmonic order.

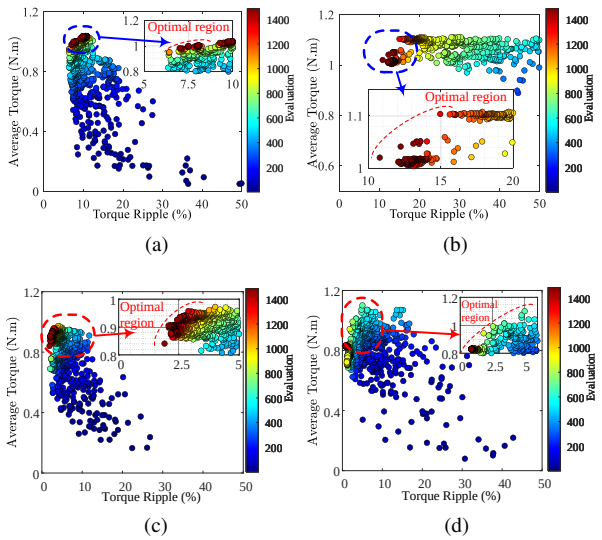

Fig. 16. Optimization results for (a) FRPM, (b) CPFRPM, (c) BFSPM, and (d) IMPM.

IV. Simulation Results

This section compares four benchmark motors together with the proposed IFRPM under no-load and full-load conditions to demonstrate the superiority of the IFRPM's topology.

A. Optimization Process

The motor design parameters, presented in Fig. 15a, are considered for optimization using a GA. By coupling the FEA with GA, 1500 structures are produced and examined. The optimization function is defined to maximize the average torque (T_{avg}) while minimizing the torque ripple (T_r) with the cost function of $0.8T_{avg} + 0.2/T_r$. In Fig. 15b, the average torque is plotted versus torque ripple, where each point represents a structure with specific motor dimensions. As the optimization progresses, the points show lower cost function values and generate more desirable outputs. The contribution of the multi-tooth structure can be revealed by investigating different stator and rotor teeth configurations. An essential step in the design methodology is to identify feasible slot/pole combinations and select the most appropriate candidates. The feasible combinations that guarantee a balanced m-phase back-EMF are defined according to the following conditions [8], [23]:

$$\frac{N_{sp}}{\mathrm{GCD}(N_{sp}, n_{rt})} = k\mathrm{m}, \tag{17}$$

where N_{sp}, N_{rt}, and m denote the stator pole number, rotor teeth number, and number of phases, respectively. Considering the vital parameters ($N_{sp} = 6$ and $m = 3$), the ratio of N_{sp} to the greatest common divisor (GCD) of N_{sp} and N_{rt} must be a multiple of three ($m = 3$ and k is an integer).

The value of N_{st} (stator teeth number) has no direct effect on determining N_{rt} (rotor teeth number) in this analysis. Therefore, values of 12, 18, and 24 were selected for N_{st}, primarily guided by structural design constraints of the motor. Selecting a higher number of stator teeth was avoided, since increasing the tooth number leads to a significant reduction in individual tooth width, which poses challenges in terms of manufacturability. For optimal performance, such as maximizing average torque and minimizing torque ripple, it is preferable for the stator and rotor tooth numbers to remain relatively close. Overall, thirteen motor configurations with different stator/rotor tooth number combinations and their optimized performances are outlined in Table IV.

TABLE IV
Optimized Characteristics of Different Stator (N_{st}) and Rotor (N_{rt}) Teeth Numbers.

N_{st}/N_{rt}	T_{avg} (Nm)	T_r (%)	TQF (Nm/cm^3)
12/10	0.72	55.5	0.2
12/11	1.02	9.6	4.3
12/13	0.95	7.5	3.5
12/14	0.43	23.5	0.3
18/16	0.8	38.1	1.1
18/17	1.1	6.9	6.1
18/19	0.9	5.0	5.5
18/20	0.5	32.1	1.5
24/20	0.6	52.1	0.2
24/22	0.6	23.5	0.5
24/23	1.0	5.0	6.2
24/25	**1.1**	**3.1**	**7.7**
24/26	0.6	117.0	0.2

TABLE V
Optimized Motor Parameters.

Parameter	Value (mm)	Parameter	Value $(deg.)$
h_{sy}	5.4	θ_{sp}	4.9°
h_{PM}	5	θ_{PM}	2.5°
h_{sp}	11.8	θ_{st}	21.5°
h_{st}	3.1	θ_{smt}	5°
h_t	2	θ_{tPM}	9.4°
h_{rt}	4.4	θ_{rt}	5°
h_{ry}	10	θ_{rs}	6°

It can be observed that by splitting the teeth, both the average torque and torque ripple are significantly improved. The splitting of teeth improves the torque ripple and average torque by 193% and 9%, respectively. Therefore, based on the global optimization results, the proposed structure with 24 stator teeth and 25 rotor teeth demonstrates the optimal performance. The optimized IFRPM parameters are listed in Table V. It is worth noting that all benchmark motors are optimized using the same optimization setup, cost function, and algorithm under an identical current density (Fig. 16).

B. No-Load Results

The flux density waveforms obtained from FEA for the air-gap under no-load conditions and the stator pole are presented in Fig. 17a and Fig. 17d, respectively. The no-load air-gap flux density of the proposed motor exhibits a 46% increase in root-mean-square (RMS) value compared to the CPFRPM. Also, under each 60° stator module, the proposed IFRPM has, on average, improved the air-gap peak-to-peak (pk2pk) value by about 30% (see Fig. 17b). The harmonics of air-gap flux density distributions of the motors are shown in Fig. 17c demonstrating that the IFRPM has a 15% enhancement in the predominant harmonics magnitude. Furthermore, the IFRPM

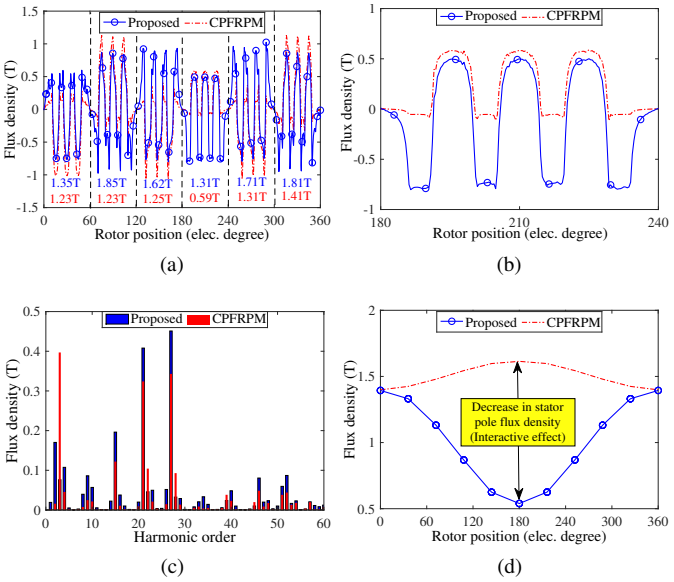

Fig. 17. Flux density comparison of (a), (b) no-load air-gap with Pk2pk values, (c) air-gap harmonic distribution, and (d) stator pole.

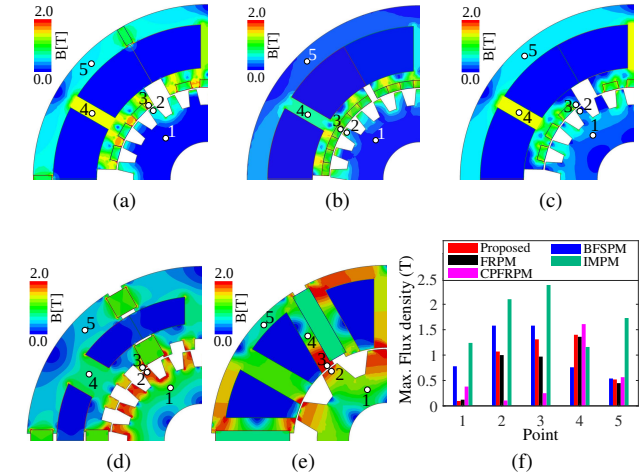

Fig. 18. No-load flux density distributions of (a) proposed IFRPM, (b) FRPM, (c) CPFRPM, (d) BFSPM, (e) IMPM, and (f) the maximum flux densities of the specified points.

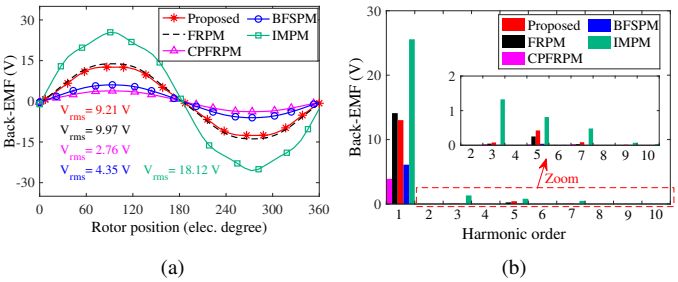

Fig. 19. (a) Back-EMF profiles. (b) back-EMF harmonics spectra.

reduces the stator pole flux density by 67%, attributed to the interactive PM configuration.

The no-load flux density distributions of the motors are illustrated in Fig. 18. It is observed that BFSPM experiences a lower flux density in the stator pole. On the other hand, IMPM shows more saturated regions than other structures. The maximum flux densities of five selected points in each motor are demonstrated in Fig. 18f. The advantage of the interactive PM arrangement can be seen in the reduction of the stator pole flux density compared to the original FRPM. The pole flux density in the proposed IFRPM remains constant compared to the CPFRPM, while the yoke PMs increase the stator/rotor teeth flux densities, resulting in a higher air gap flux density with no exposure to saturation. The back-EMF profiles and their harmonic spectra are shown in Figs. 19a and 19b, respectively. The IFRPM presents a sinusoidal waveform with a 9.21V root-mean-square (RMS) value and 3.3% total harmonic distortion (THD). Although IMPM has twice the RMS back-EMF, it has a THD of 6.3%, the highest among the motors. The FRPM, BFSPM, and CPFRPM produce sinusoidal back-EMF waveforms with a 9.97V, 4.35V, and 2.76V RMS value, respectively. The IFRPM has the smallest cogging torque (Fig. 20), with a peak-to-peak amplitude of 11mNm. In contrast, the FRPM and IMPM motors show approximately six times higher cogging torque than the IFRPM motor.

C. Full-Load Results

Since the motor is designed with natural cooling, the current density is selected as $6A/mm^2$. The full-load flux density distributions of the motors are shown in Fig. 21. The impact of placing yoke PMs in the IFRPM structure can be demonstrated by comparing the IFRPM and CPFRPM machines. The comparison reveals that the stator poles of the CPFRPM are saturated due to the absence of yoke PMs, whereas the proposed IFRPM exhibits improved magnetic performance with reduced saturation (see Figs. 21a and 21c). Furthermore, the volume and arrangement of the PMs in the IFRPM do not cause stator saturation, whereas the IMPM experiences saturation in the yoke, poles, and teeth due to its PM configuration and volume. Overall, the IFRPM demonstrates the lowest risk of magnetic saturation among the compared benchmark designs.

The IFRPM, IMPM, and CPFRPM have the same average torque of 1.1N.m (Fig. 22a). However, the IFRPM has the lowest ripple of 3.3% among these three motors. Furthermore, FRPM and BFSPM have 9% and 15% lower average torques compared to the IFRPM. For a better evaluation, the PM volume (V_{PM}) and torque ripple are considered in torque comparison by introducing a metric called the torque quality factor (TQF), defined as $TQF = \dfrac{T_{avg}/V_{PM}}{T_r} \times 100$. The TQF metric for different current densities is plotted in Fig. 22b. The TQF of the IFRPM has significantly improved, showing an increase of 95%, 318%, 669%, and 1418% compared to CPFRPM, BFSPM, FRPM, and IMPM, respectively.

In order to investigates the torque contribution from each PM array (yoke and tooth PMs), the frozen permeability method is used. The frozen permeability approach accounts for the nonlinear B-H behavior of the iron material under nominal load conditions by using the material's permeability corresponding to the nominal current. Additionally, by using this technique, the sum of the torque generated by each PM

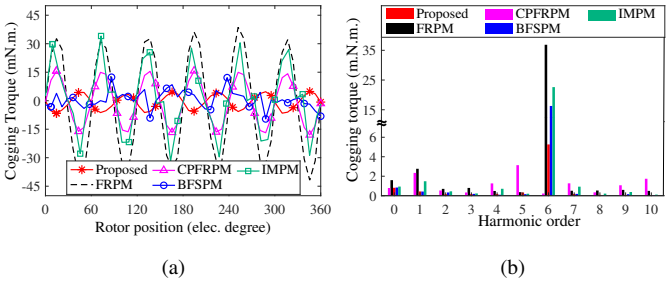

Fig. 20. (a) Cogging torque. (b) Cogging torque harmonic spectra.

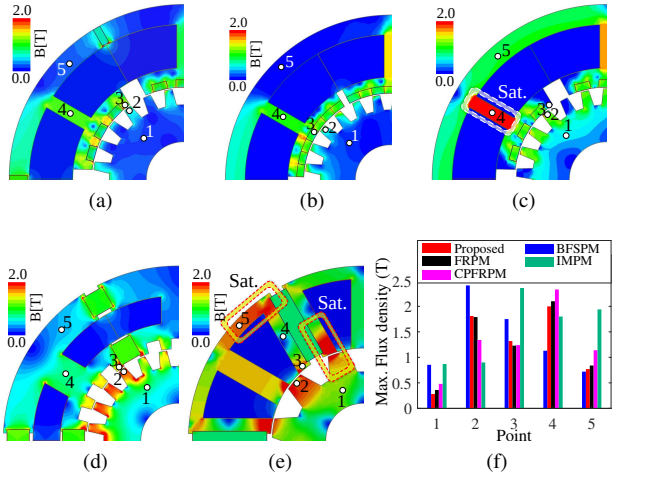

Fig. 21. Full load flux density distributions of (a) proposed IFRPM, (b) FRPM, (c) CPFRPM, (d) BFSPM, (e) IMPM, and (f) the maximum flux densities of the specified points.

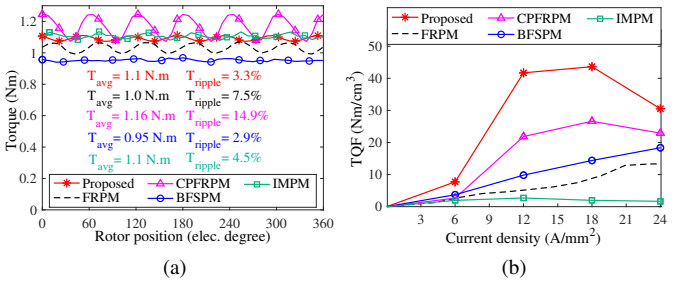

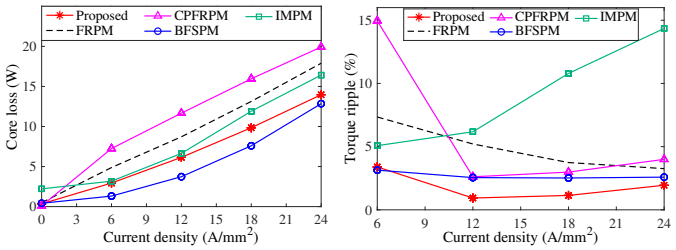

Fig. 22. (a) Full-load torque profiles. (b) TQF performance, (b) average core loss, and (c) torque ripple versus current density profiles.

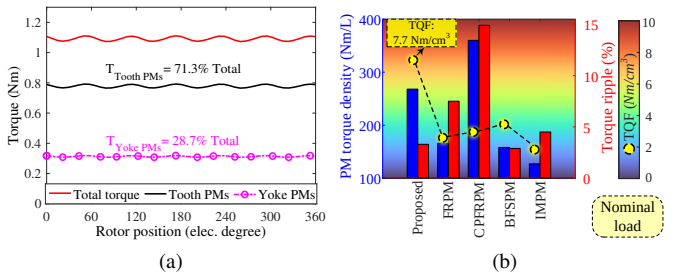

Fig. 23. (a) On-load torque and torque synthesis using frozen permeability method. (b) TQF performance comparison.

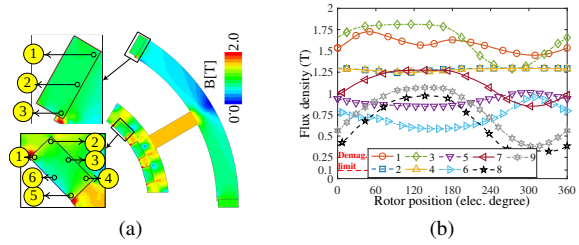

Fig. 24. PM demagnetization analysis at the temperature of 80°C. (a) Flux density distribution. (b) Flux density curves of different points.

array constitutes the actual full-load torque, and the corresponding torque generation profiles are shown in Fig. 23a. The torque synthesis shows that the individual contributions of the yoke and tooth PMs account for 28.7% and 71.3% of the total torque generation, respectively. It can be observed that both PM arrays have a significant impact on the full-load torque; however, the torque generated by the tooth PMs (FR effect) is approximately twice as high as that generated by the yoke PMs (BF effect). Additionally, Fig. 23b presents the motors' different parameters under nominal current density to have a general comparison. Although the IFRPM and CPFRPM exhibit the highest PM torque densities, the IFRPM has a torque ripple that is less than one-fifth of the CPFRPM torque ripple. This enables the IFRPM to outperform other motors in terms of the TQF metric, achieving a value of 7.7 Nm/cm^3, nearly a 100% improvement compared to other motors. This result indicates that, in addition to possessing a high PM torque density, the IFRPM also demonstrates a low torque ripple.

The average core losses under different loads are illustrated in Fig. 22c. At the nominal load, the core losses of BFSPM, the IFRPM, IMPM, FRPM, and CPFRPM are 1.3W, 2.9W, 3.2W, 4.9W, and 7.2W, respectively. The same scenario exists for overload conditions as well. It should be noted that although BFSPM has a lower core loss, it delivers 13% less torque and output power compared to the IFRPM. Furthermore, by comparing the FRPM-type motors (FRPM and CPFRPM) with the IFRPM, the interactive array has resulted in a 40% and 59% reduction in core loss. In addition, the IFRPM offers a torque ripple of maximum 3.3% across all loads, the lowest among all, as presented in Fig. 22d.

In the IFRPM, five points on the edge of the PMs are selected, which are more vulnerable than the central regions, shown in Fig. 24a. Given that the chosen PM material is NdFeB-N42, which has a demagnetization threshold of 0.1T at the temperature of 80°C, the maximum flux density is 0.32T, as demonstrated in Fig. 24b. This indicates that there is no

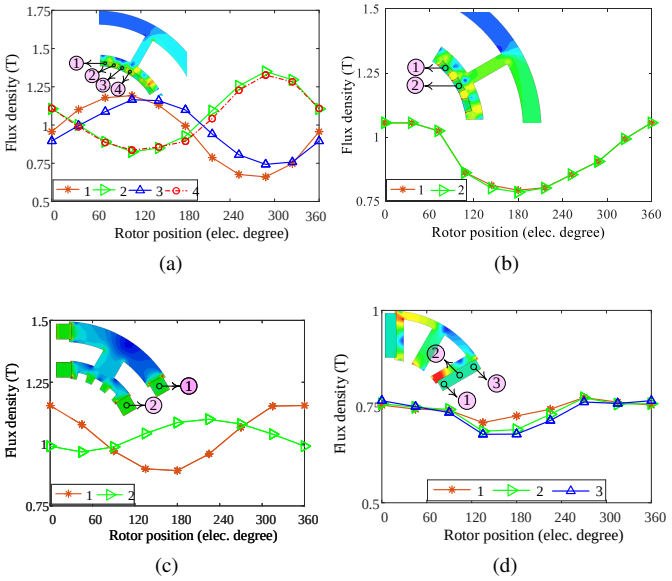

Fig. 25. PM demagnetization analysis at the temperature @ 80°C. (a) FRPM. (b) CPFRPM. (c) BFSPM. (d) IMPM.

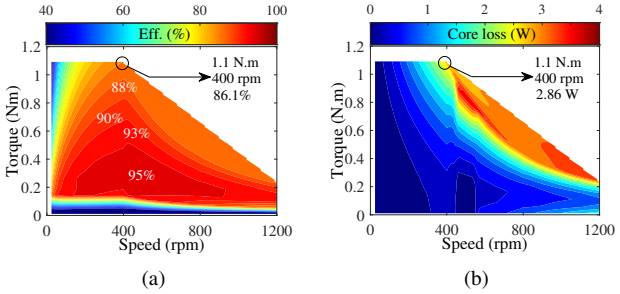

Fig. 26. (a) Efficiency and (b) core loss map of the IFRPM.

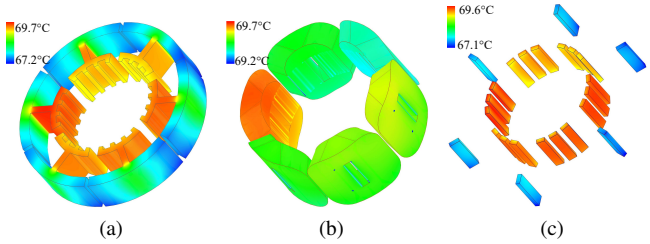

Fig. 27. The temperature distribution in stationary parts of the motor (main parts in the heat source). (a) Stator. (b) Coils. (c) PMs.

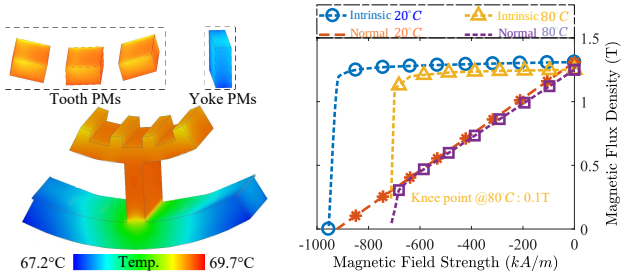

Fig. 28. (a) Close-up view of the temperature distribution in the stator module and PMs. (b) NdFeB-N42 material $B-H$ curve.

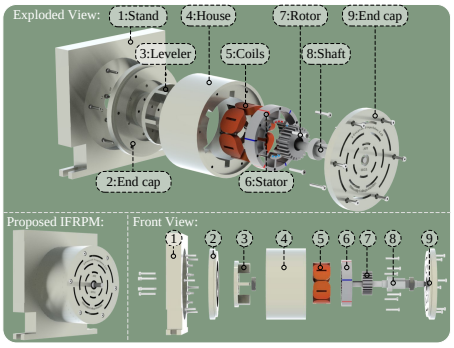

Fig. 29. Three-dimensional exploded view of the IFRPM.

demagnetization risk for the PMs. For the other motors, the flux density (under full-load condition), specifically the PMs flux densities distributions, are shown in Fig. 25. The points are placed in the vulnerable regions in the PMs. At 80°C, the working temperature of the motors, all points operate at a safe condition and far from demagnetization limitation.

The efficiency and core loss maps of the IFRPM are plotted in Figs. 26a and 26b, respectively. In the efficiency map, the area with efficiencies greater than 90% covers 65% of the map's surface. Furthermore, the region with efficiency higher than 80% accounts for 90% of the map's area, indicating that the motor maintains a high efficiency at most of the operating points. For the core loss map, over 87% of the area has a core loss below 1W. At the nominal point, the motor has 2.86W of core loss with an efficiency of 86.1%.

Under nominal conditions and natural convection, the temperature distribution across various parts of the motor (stator, coils, and PMs) that are exposed to the heat source (windings) is illustrated in Fig. 27. The temperature profile is presented for the steady-state condition, particularly when the core losses have reached thermal equilibrium. No part of the motor structure exceeds 70°C under steady-state conditions. Due to the placement of the excitation coils on the stator, the stationary components, including the stator, coils, and PMs, reach an average temperature of approximately 68.5°C. Furthermore, this operating temperature can be significantly reduced by employing a forced convection cooling method.

To provide a more detailed analysis, the temperature distribution for a single stator module is illustrated in Fig. 28a. It can be observed that no region exceeds 69.7°C, and the other modules exhibit lower temperatures than the one shown. The thermal analysis confirms that all regions of the motor, including the PMs, operate at temperatures below 80°C. The B-H curve for the NdFeB-N42 PM material and its demagnetization limit are evaluated at 80°C, verifying the motor's performance and the PMs' reliable operation under this condition. The B-H characteristic and demagnetization limit of the PM material are illustrated in Fig. 28b.

V. Experimental Verifications

A detailed illustration of the prototyped motor assembly is presented in Fig. 29. Fig. 30a shows the rotor and stator

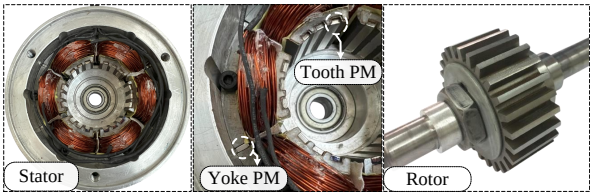

(a)

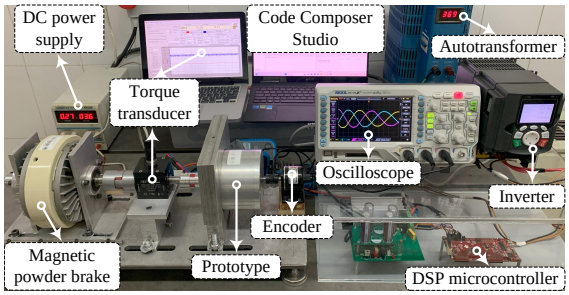

(b)

Fig. 30. (a) IFRPM Motor prototype. (b) The test rig.

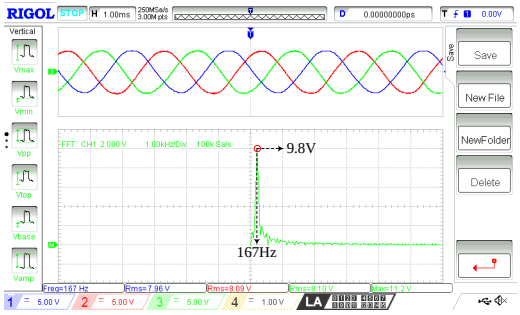

Fig. 31. Measured 3-phase back-EMF waveforms at 400rpm.

prototypes with the yoke/tooth PMs and concentrated windings. Furthermore, the test rig is shown in Fig. 30b. The q-axis current is controlled by the inverter, which injects the nominal three-phase current into the windings. Additionally, the motor is coupled to a magnetic powder brake through a torque transducer. The experimental back-EMF waveform at 400rpm is demonstrated in Fig. 31a. The experimental waveform has an 8.2V RMS value with 3.5% THD, which indicates less than 10% error compared to 2D-FEA due to end effects and manufacturing tolerances. Therefore, the 3D-FEA-obtained back-EMF is compared to the waveforms and shown in Fig. 32. Comparing the 3D-FEA curve with experimental results, an impressive accuracy with an error margin of less than 4% at various speeds is observed (Figs. 32a and 32b).

The experimental torque waveform is compared with FEA results in Fig. 33a. The motor operates with 1.05Nm average torque and 4.7% ripple, showing less than 4% error compared to the FEA results. For further verification of FEA results, Fig. 33b demonstrates the motor efficiency at various speeds and torque values as discrete points. Additionally, the errors of these points compared to the FEA results are represented as a gray-scale map. At full load, the motor has 82.61% efficiency. The error between FEA and test results remains below 4%, confirming the agreement between the FEA and test results.

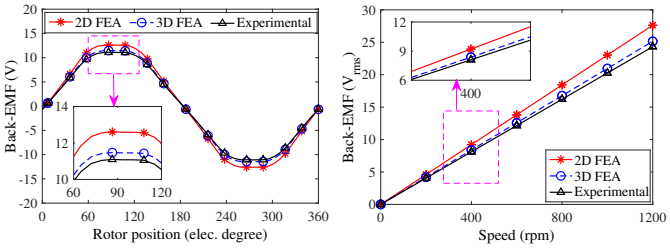

(a) (b)

Fig. 32. Comparison of 2D, 3D FEA, and experimental back-EMF profiles (a) at 400rpm and (b) RMS values versus speed.

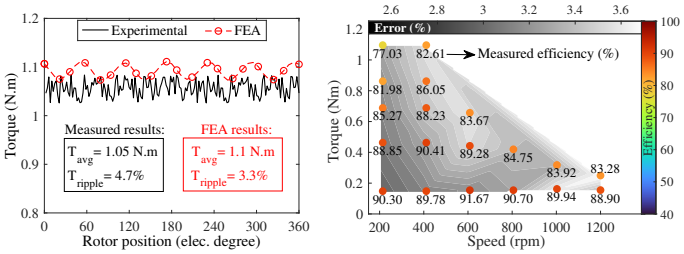

(a) (b)

Fig. 33. Experimental results. (a) Torque. (b) efficiency and error map.

The IFRPM prototype shows a power factor that peaks near 0.50 at rated current, consistent with typical stator-PM/FRPM motors. At the rated point, measured losses were 4.6 W (copper), 3.0 W (core), and 0.4 W (mechanical), yielding an output power of 42.5 W and efficiency of about 82.6%, with notably low mechanical losses due to the rotor design.

VI. Conclusion

This article proposed a new multi-tooth interactive flux reversal permanent magnet (IFRPM), which effectively reduced the pole flux density while increasing the air gap flux density. By performing flux modulation theory (FMT), the contribution of the harmonics generated by interactive PMs to back-EMF and torque generation is unveiled. Four benchmark motors with only the BF or FR effect are introduced to be compared with the optimized IFRPM. The IFRPM improved the torque quality (TQF) factor by 95% and 669% compared to Consequent-pole FRPM and conventional FRPM, indicating a substantial increase in torque per PM volume and an improvement in torque ripple at the same time. Moreover, the novel IFRPM outperformed the biased flux motor, exhibiting an improved TQF that is at least 318% higher. Thermal analysis showed that the proposed motor maintains a safe operating temperature below 70°C. Finally, to validate the FEA results, the IFRPM is manufactured and rigorously tested under various torques and speeds. These tests confirmed the accuracy of the analytical and simulation findings.

References

[1] J. Huang, W. Fu, S. Niu, X. Zhao, and Y. Bi, "A novel dual-side pm machine with decoupled stator pm topology," *IEEE Transactions on Industrial Electronics*, vol. 71, DOI 10.1109/TIE.2024.3383009, no. 12, pp. 15 301–15 312, 2024.

[2] E. F. Farahani, M. A. J. Kondelaji, and M. Mirsalim, "An innovative hybrid-excited multi-tooth switched reluctance motor for torque enhancement," *IEEE Transactions on Industrial Electronics*, vol. 68, DOI 10.1109/TIE.2020.2969073, no. 2, pp. 982–992, 2021.
[3] M. Cheng, W. Hua, J. Zhang, and W. Zhao, "Overview of stator-permanent magnet brushless machines," *IEEE Transactions on Industrial Electronics*, vol. 58, DOI 10.1109/TIE.2011.2123853, no. 11, pp. 5087–5101, 2011.
[4] Y. Bi, W. Fu, S. Niu, X. Zhao, and J. Huang, "Design of a dual-set permanent magnet flux-switching machine with enhanced torque density and fault-tolerance capability," *IEEE Transactions on Transportation Electrification*, DOI 10.1109/TTE.2023.3346820, pp. 1–1, 2023.
[5] J. Shi, Z. Zhu, D. Wu, and X. Liu, "Comparative study of biased flux permanent magnet machines with doubly salient permanent magnet machines considering with influence of flux focusing," *Electric Power Systems Research*, vol. 141, DOI 10.1016/j.epsr.2016.07.023, pp. 281–289, 12 2016.
[6] R. Deodhar, S. Andersson, I. Boldea, and T. Miller, "The flux-reversal machine: a new brushless doubly-salient permanent-magnet machine," *IEEE Transactions on Industry Applications*, vol. 33, DOI 10.1109/28.605734, no. 4, pp. 925–934, 1997.
[7] M. Amirkhani, E. F. Farahani, and M. Mirsalim, "Study of an improved biased-flux intermodular permanent magnet motor," *IEEE Transactions on Transportation Electrification*, vol. 10, DOI 10.1109/TTE.2023.3310449, no. 2, pp. 4455–4469, 2024.
[8] M. Amirkhani, M. A. J. Kondelaji, A. Ghaffarpour, M. Mirsalim, and S. Vaez-Zadeh, "Study of boosted toothed biased flux permanent magnet motors," *IEEE Transactions on Transportation Electrification*, vol. 8, DOI 10.1109/TTE.2022.3141331, no. 2, pp. 2549–2564, 2022.
[9] W. Liu, H. Yang, H. Lin, and L. Qin, "Hybrid analytical modeling of air-gap magnetic field in asymmetric-stator-pole flux reversal permanent magnet machine considering slotting effect," *IEEE Transactions on Industrial Electronics*, vol. 69, DOI 10.1109/TIE.2021.3062265, no. 2, pp. 1739–1749, 2022.
[10] H. Yang, Z. Q. Zhu, H. Lin, H. Li, and S. Lyu, "Analysis of consequent-pole flux reversal permanent magnet machine with biased flux modulation theory," *IEEE Transactions on Industrial Electronics*, vol. 67, DOI 10.1109/TIE.2019.2902816, no. 3, pp. 2107–2121, 2020.
[11] H. Qu, Z. Q. Zhu, and H. Li, "Analysis of novel consequent pole flux reversal permanent magnet machines," *IEEE Transactions on Industry Applications*, vol. 57, DOI 10.1109/TIA.2020.3036328, no. 1, pp. 382–396, 2021.
[12] Y. Zheng, W. Xiang, H. Xu, P. Tan, and Y. Fang, "Analysis of a flux reversal machine with consequent-pole evenly distributed pm," *IEEE Transactions on Industry Applications*, vol. 60, DOI 10.1109/TIA.2023.3269738, no. 1, pp. 4–11, 2024.
[13] H. Hua and Z. Q. Zhu, "Investigation on symmetrical characteristics of consequent-pole flux reversal permanent magnet machines with concentrated windings," *IEEE Transactions on Energy Conversion*, vol. 37, DOI 10.1109/TEC.2022.3141554, no. 3, pp. 1815–1824, 2022.
[14] K. Xie, D. Li, R. Qu, Z. Yu, Y. Gao, and Y. Pan, "Analysis of a flux reversal machine with quasi-halbach magnets in stator slot opening," *IEEE Transactions on Industry Applications*, vol. 55, DOI 10.1109/TIA.2018.2873540, no. 2, pp. 1250–1260, 2019.
[15] K. Yang, F. Zhao, Y. Wang, and Z. Bao, "Consequent-pole flux reversal permanent magnet machine with halbach array magnets in rotor slot," *IEEE Transactions on Magnetics*, vol. 57, DOI 10.1109/TMAG.2020.3007861, no. 2, pp. 1–5, 2021.
[16] H. Yang, H. Lin, Z. Q. Zhu, S. Lyu, and Y. Liu, "Design and analysis of novel asymmetric-stator-pole flux reversal pm machine," *IEEE Transactions on Industrial Electronics*, vol. 67, DOI 10.1109/TIE.2019.2896097, no. 1, pp. 101–114, 2020.
[17] F. Wei, Z. Q. Zhu, X. Sun, L. Yan, and J. Qi, "Investigation of asymmetric consequent-pole hybrid excited flux reversal machines," *IEEE Transactions on Industry Applications*, vol. 58, DOI 10.1109/TIA.2022.3151316, no. 3, pp. 3434–3446, 2022.
[18] F. Wei, Z. Zhu, L. Yan, and J. Qi, "Investigation of stator/rotor pole number combinations and pm numbers in consequent-pole hybrid excited flux reversal machine," *IEEE Transactions on Energy Conversion*, vol. 37, DOI 10.1109/TEC.2022.3163654, no. 3, pp. 2092–2106, 2022.
[19] L. Xu, G. Liu, W. Zhao, X. Yang, and R. Cheng, "Hybrid stator design of fault-tolerant permanent-magnet vernier machines for direct-drive applications," *IEEE Transactions on Industrial Electronics*, vol. 64, DOI 10.1109/TIE.2016.2610399, no. 1, pp. 179–190, 2017.
[20] T. Jiang, W. Zhao, and L. Xu, "Analysis of split-tooth stator pm vernier machines with zero-sequence current excitation," *IEEE Transactions on Industrial Electronics*, vol. 70, DOI 10.1109/TIE.2022.3161757, no. 2, pp. 1229–1238, 2023.
[21] S. Cai, H. Chen, X. Yuan, Y.-C. Wang, J.-X. Shen, and C. H. T. Lee, "Analysis of synergistic stator permanent magnet machine with the synergies of flux-switching and flux-reversal effects," *IEEE Transactions on Industrial Electronics*, vol. 69, DOI 10.1109/TIE.2021.3134063, no. 12, pp. 12 237–12 248, 2022.
[22] Y. Bi, W. Fu, S. Niu, X. Zhao, J. Huang, and Z. Qiao, "Torque enhancement of a dual-pm flux-switching machine with improved multiple high-order working harmonics," *IEEE Transactions on Transportation Electrification*, vol. 10, DOI 10.1109/TTE.2023.3294189, no. 2, pp. 2830–2843, 2024.
[23] M. R. Sarshar, M. A. J. Kondelaji, J. Kavianpour, and M. Mirsalim, "Split-tooth flux reversal motor assisted with yoke and slot pms," *IEEE Transactions on Transportation Electrification*, DOI 10.1109/TTE.2025.3567397, pp. 1–1, 2025.

Mohammad Amin Jalali Kondelaji was born in Marand, Iran, in 1994. He received the B.Sc. and M.Sc. degrees in electrical engineering from the Amirkabir University of Technology (Tehran Polytechnic), Tehran, Iran, in 2016 and 2019, respectively. Currently, he is an electrical machines and systems specialist at APL within the Department of Mechanical Engineering at University College London (UCL). His expertise includes the design, electromagnetic modeling, and prototyping of advanced electric motors.

Mohammad Reza Sarshar was born in Tehran, Iran, in 2000. He received the B.Sc. and M.Sc. degrees (with first class honor) both in electrical engineering from Amirkabir University of Technology (Tehran Polytechnic), Tehran, Iran, in 2022 and 2025, respectively. Currently, he is working as a postgraduate research assistant at the Electrical Machines and Transformers Research Laboratory (EMTRL), Amirkabir University of Technology (Tehran Polytechnic).

Pedram Asef (SM'21) received his Ph.D. degree (cum laude) in Electrical Engineering from Polytechnic University of Catalonia (UPC), Barcelona, Spain, in 2019. He is currently an Assistant Professor of Advanced Electrical Machines with the Department of Mechanical Engineering, UCL. He is a Co-Director of the e-Motion Laboratory and a member of the Advanced Propulsion Laboratory at UCL. He is a Panel Member of the Royal Society and British Council for Grant Application Assessment.

Mojtaba Mirsalim (SM'04) received the B.S. degree in double major electrical/nuclear engineering and the M.S. degree in nuclear engineering from the University of California at Berkley, Berkley, CA, USA, in 1978 and 1980, respectively, and the Ph.D. degree in electrical engineering from Oregon State University, Corvallis, OR, USA, in 1986. He is a Full Professor at AUT, Tehran, Iran, and serves as an editor of the *IEEE TEC*.